Permeability and compaction behaviour of air-texturised glass fibre rovings: A characterisation study

Journal Article

Author(s):
Sandberg, Michael; Kabachi, Ayyoub; Volk, Maximilian; Bo Salling, Filip; Ermanni, Paolo; Hattel, Jesper H.; Spangenberg, Jon

Publication date:
2020-11-01

Permanent link:
https://doi.org/10.3929/ethz-b-000418129

Originally published in:
Journal of Composite Materials 54(27), https://doi.org/10.1177/0021998320926703

Permeability and compaction behaviour of air-texturised glass fibre rovings: a characterisation study

Journal of Composite Materials
XX(X):2–??

DOI: 10.1177/ToBeAssigned
www.sagepub.com/
SAGE

Michael Sandberg[1], Ayyoub Kabachi[2], Maximilian Volk[2], Filip Bo Salling[1], Paolo Ermanni[2], Jesper H. Hattel[1], and Jon Spangenberg[1]

Abstract

Air-texturisation is a process that adds bulkiness to bundles of fibres. In this study, the permeability and compaction behaviour of air-texturised glass fibre rovings are experimentally characterised and compared to conventional unidirectional (UD) rovings. Based on radial impregnation experiments and single-step compaction/decompaction tests, the following main findings are highlighted: Compared to conventional UD-rovings, the normalised permeability of the air-texturised rovings was approximately three times higher along the fibre direction and 40 times higher transverse to the fibre direction. Accordingly, the degree of anisotropy was approximately one magnitude lower. At a compaction pressure of 1 and 5 bar, the air-texturised rovings were compacted to a volume fraction of $V_f = 0.34$ and 0.43, respectively, which was approximately 30% lower than the volume fraction achieved for the conventional UD-rovings. Finally, it was observed that the decompaction of air-texturised rovings exhibits a more distinct elastic response when unloaded.

Keywords

Permeability; Compaction; Texturisation; Rovings; Liquid composite moulding

Nomenclature

A_w	Areal weight
A_s	Spring constant, or fitting parameter
$\dot{h}$	Displacement rate of crosshead
h	Cavity thickness in permeability cell and distance between discs in compaction tests
K'	Quasi-isotropic permeability
k_1	Constant in power law
K_i, ψ	Principal permeabilities and direction
μ	Viscosity
n_i	Exponents in power law
p	Pressure
p_i	Pressere at pressure sensor i
p_{in}	Inlet pressure
Q	Inflow rate
ρ_f	Density of fibres
r	Radius, radial coordinate
r_f	Radial distance to flow front
R_f	Fibre radius
r	Radius of inlet
t	Time
$\mathbf{u}$	Velocity
V_f	Fibre volume fraction
V_0	Fibre volume fraction for sample at rest, or fitting parameter
V_a	Maximum available fibre volume fraction, or fitting parameter
x_i, x'_i	Spatial coordinates, global and local

Introduction

Impregnation flow is governed by the ability of fibrous materials to transmit a fluid during impregnation (the permeability) as well as the mechanical response when subject to a pressure state (the compaction behaviour defined as the constitutive relation between stress and strain or volume fraction). In liquid composite moulding (LCM) processes, most fibre-reinforced composite parts are composed of a layup of fabrics, mats, and flow media. By designing a layup of appropriate fibre architectures, engineers can time the impregnation step to a suitable process window. In pultrusion, which belongs to the family of LCM processes, a layup can consist of rovings of fibres[1–4]. Here, instead of controlling the local permeability by selecting special types of fabrics or mats, permeability can be altered by applying texturisation to rovings. Air-texturised rovings can also be combined with matrix-forming filaments to form a commingled yarn, braided into technical fabrics, or directly enter the fibre layup in other continuous composite manufacturing processes.

[1]Department of Mechanical Engineering, Technical University of Denmark
[2]Laboratory of Composite Materials and Adaptive Structures, ETH Zürich

Corresponding author:
Produktionstorvet, Building 425, Room 225, DK-2800 Kgs. Lyngby, Denmark
Email: misan@mek.dtu.dk

In air-texturisation, one or more bundle of fibres are drawn through an air-jet nozzle, which creates a clutter of individual fibres and adds volume to the roving. The resulting roving is suitable for applications where a lower fibre volume fraction is desired and fast resin impregnation is critical. Fast impregnation flow is crucial for thick composite parts and a low fibre volume fraction can be a cost-wise desired choice for non-structural parts.

As the aforementioned characteristics are distinct features of air-texturised rovings, it is important to quantify what the effect of applying texturisation has on the impregnation flow when used in LCM processes. To the authors' knowledge, there exists no such characterisation studies of air-texturised rovings in the current literature and this study seeks to bridge this gap. As the focus of this study is permeability and compaction behaviour, we briefly review some of the existing literature concerning conventional fibrous materials.

State-of-the-art

Early models of compaction behaviour are based on the concept that bundles of fibres are essentially aligned cylinders with multiple contact points. Following this terminology, Gutowski et al.[5,6] introduced an analytical model for the quasi-static nonlinear stress-strain behaviour of a bundle of fibres in terms of the compaction pressure. Essentially, Gutowski et al.'s model describes the relationship between the compaction pressure, σ, and the volume fraction, V_f, using a power-law function. The function is bounded by horizontal and vertical asymptotes, which correspond to at some level the fibrous material is a rest, $\sigma \to 0$, and at another level, a maximum fibre volume fraction is achieved, $V_f \to V_a$. In this context, V_a is often referred to as the "maximum available fibre volume fraction", and is related to the densest possible fibre packing in the fibrous material. In experiments, Gutowski et al.[5] showed that misaligned (i.e. disordered) fibres will generally have a lower V_a-value.

While other researchers have explored and developed additional compaction models for unidirectional fibres and fabrics[7–10], generic polynomial expansions can also be applied for fitting experimental data[11–13]. The model proposed by Gutowski et al.[5,6] is suitable for a fibrous material exhibiting fully elastic behaviour, which means it provides a good fit for a fibre compaction without any subsequent unloading. Researchers have later reported that the response of fibrous materials exhibits both inelastic and time-dependent behaviour. These effects include irreversible deformation[14,15] and viscoelastic effects[16,17]. Furthermore, repeated loading and unloading yield a hysteresis with cyclic softening[18,19].

For a bank of aligned fibres, there exist several semi-empirical models for estimating the permeability. These models are based on an idealised hexagonal or square packing of fibres, and their empirical background is commonly established using CFD simulations. While there are differences between the various models, permeability is seen to scale proportionally to the fibre radius squared, R_f^2, and to decrease with increasing fibre volume fraction, V_f[20–24]. In addition, models have shown that the permeability increases with increasing disordering of fibre packing[25,26].

Obviously, a bank of aligned cylinders is a poor representation of many fibre architectures, including many fabrics and mats. Consequently, conducting impregnation and compaction experiments is a necessity for material characterisation of many fibrous materials. As layups of mats and fabrics resemble the ply configuration in many LCM processes, several setups for this type of material characterisation can be found in the literature. For permeability characterisation, special moulds have been designed for controlled linear or radial impregnation experiments (see e.g.[27–29]). Similarly, for compaction experiments, a conventional universal testing machine can be used to test the compaction behaviour of a layup of fabrics or mats[17,19]. For some LCM processes, a layup is not necessarily composed of fabrics or mats, but of single rovings. This can be the case in pultrusion processes, where individual rovings are drawn directly through the pultrusion die. In such a layup, rovings are not intertwined or bound by back-threading. A few studies of this type of layup can also be found in the literature. For example, Schell et al.[30] were able to measure the longitudinal and transverse permeability of this fibre configuration using a special mould enclosing a single roving. Bezerra et al.[31,32] designed a setup intended to represent pultrusion processes. In this setup, rovings are guided through a permeability cell or compaction mould using perforated plates. This system fixates the stack of rovings while impregnation (radial) or compaction experiments take place.

Scope

Based on the literature review in this section, we briefly discuss how air-texturisation is expected to affect the permeability and compaction behaviour of rovings. For this purpose, X-ray μ-CT scans of composite parts prepared with conventional UD-rovings as well as air-texturised rovings are depicted in Fig. 1. A description of how these scans were conducted can be found in Rasmussen et al.[33] and a summary is given in Appendix A.

As illustrated in Fig. 1, the fibre architecture of the part prepared with conventional UD-rovings has a high degree of uniformity. This configuration is seen to be well-represented by the concept that a bundle of fibres is essentially cylinders with multiple contact points. On the other hand, the part prepared with air-texturised rovings has a very disordered fibre architecture. The texturisation process introduces out-of-plane fibres as individual fibres cross over and intertwine. In addition, there are several areas with highly agglomerated fibres that increase the non-uniformity of fibre distribution as the figure illustrates.

In summary, the increased disorder in the fibre architecture is expected to increase the permeability[25,26] as well as decrease the compliance by lowering the ”available fibre volume fraction”[5,6].

[Figure 1 around here]

Method

Sample preparation

To prepare a layup where rovings were not intertwined or bound by back threading, rovings were drawn through two fibre guides mounted on a rack. See Fig. 2(a). The fibre guides were two polypropylene plates which were perforated with a hole pattern corresponding to the typical equipment used in pultrusion processes[32]. This pattern aligned five rovings per 15 mm. Essentially, this procedure was similar to Bezerra et al.[31,32], but instead of drawing rovings from individual bobbins, a single roving was drawn back and forth between the two perforated plates. This simplified the setup as the number of bobbins needed was reduced from between 50-100 to a single bobbin.

[Figure 2 around here]

After the layup of rovings was prepared in the rack, a small amount of a powder soluble (approximately 2 g/sample of FILCO 661MG020, Coim) was sprinkled on the locations that were excess to the area in contact with the testing machine (Fig. 2(a)). This area was subsequently heated with a heat gun and clamped. Finally, an inlet hole ($r = 7.5$ mm) was cut (ZUND M1600 CNC textile cutting machine) in the samples for permeability tests, see Fig. 2(b). To ensure the inlet hole dimensions, the samples were placed on a vacuum table and cut beneath a vacuum foil. This preparation method gave a ply-like sample of rovings, where the testing area was unaffected of the processing steps.

Permeability experiments

The prepared sample was placed inside a permeability cell designed for radial injection tests. The permeability cell consisted of a 40 mm thick top and bottom solid steel plates. An industrial type press (30 tonnes) was used to close the top and bottom plate, and mechanical spacers ensured the cavity thickness (h). The setup can be seen in Fig. 3(a).

[Figure 3 around here]

Through the inlet hole, a test fluid (Bluesil 47 V 100, 40-123.KN.K025, $\mu = 0.1$ Pa·s) was pumped into the centre of the sample at a constant injection rate. To verify that the dimensions and shape had not changed during impregnation, the inlet hole was visually inspected before and after the experiments. While the impregnation took place, seven pressure sensors in the bottom plate of the permeability cell continuously monitored the development in fluid pressure. Six of the sensors were located in a radial pattern on one-half of the bottom plate and one sensor was positioned at the inlet (see Fig. 3(b)).

As the method for estimating the permeability in this paper was based on the work by Louis et al.[34], only a summary of the approach is given below. Please note that the same setup was used in a recent benchmark exercise, see May et al.[29].

The permeability measurements were based on closed-form solutions of Darcy's law for creeping flow in porous media assuming a fully developed saturated zone, constant fluid viscosity, incompressible fluid, rigid fibrous material, and a negligible level of capillary pressure. Darcy's law states that the fluid velocity, $\mathbf{u}$, scales proportionally to the fluid pressure gradient:

$$(1 - V_f)\mathbf{u} = \frac{\mathbf{K}}{\mu}\nabla p \tag{1}$$

where $\mathbf{K}$ is permeability tensor of the fibrous material and μ is the viscosity of the fluid. The volume fraction was calculated based on the areal weight of each sample, A_w, and the cavity thickness in the testing machine, h, specifically:

$$V_f = \frac{A_w}{\rho_f h} \tag{2}$$

where ρ_f is the density of fibres ($\rho_f = 2550$ kg·m^{-3}, E-glass fibres).

The fibrous material will in this relation be referred to as the porous medium and it is characterised with principal permeabilities, K_1 and K_2. These permeabilities apply for the orientation angle, ψ, where off-diagonal terms in the permeability tensor $\mathbf{K}$ are zero. For aligned fibres, K_1 follows the fibre direction and K_2 is transverse to the fibre direction. The analytical solution for the radial impregnation flow in an anisotropic porous medium was based on a coordinate transformation of the anisotropic domain into a quasi-isotropic domain[35,36]. The quasi-isotropic permeability and the coordinate transformation follow the relation (see Fig. 3(b)):

$$K' = \sqrt{K_1 K_2}, \quad x_1' = \sqrt{K'/K_1}x_1, \quad x_2' = \sqrt{K'/K_2}x_2 \tag{3}$$

In the quasi-isotropic domain, the flow front develops in the shape of a circle. By simple geometrical considerations, a relation between time, t, and the radius of this circle, r_f, was established:

$$r_f(t) = \sqrt{\frac{Qt}{\pi(1 - V_f)h} + r_{in}^2} \tag{4}$$

where Q is the inflow rate of the test fluid. The pressure at the inlet was found using the relation:

$$p_{in}(t) = \frac{Q\mu}{4\pi h K'} \ln\left(1 + \frac{Qt}{(1 - V_f)\pi h r_{in}^2}\right) \tag{5}$$

Once the inlet pressure and flow front radius, r_f, was determined, the pressure level within the saturated domain was estimated as:

$$p(r,t) = p_{in}(t)\left(1 - \frac{\log(r/r_{in})}{\log(r_f/r_{in})}\right) \quad (6)$$

The estimated pressure level in the saturated domain was then mapped to individual sensor locations, $p(x_i, y_i)$, using the principal direction, ψ, and the coordinate transformation in Eq. (3). Finally, the principal permeabilities and direction, K_1, K_2, and ψ, were determined by minimising the sum of squared residuals wrt. the measured pressure level of sensor i, $p_{i,exp}$:

$$\text{Residual} = \sum_{i}^{n_{sensor}} \left(p_{i,exp} - p(x_i, y_i)\right)^2 \quad (7)$$

where n_{sensor} is the number of pressure sensors. As the impregnation took place and the impregnated zone expanded, the principal permeabilities and direction, K_1, K_2, and ψ converged. The reported values of K_1, K_2, and ψ were taken as average values of the last 10 seconds in each experiment.

After the permeabilities at different volume fractions were determined, Gebart's model[21], Eq. (8), was fitted by calculating a best-fit fibre radius, R_f:

$$K_1 = \frac{8}{53}\frac{(1-V_f)^3}{V_f^2}R_f^2, \quad K_2 = \frac{16}{9\pi\sqrt{6}}\left(\sqrt{\frac{V_a}{V_f}} - 1\right)^{\frac{5}{2}} R_f^2 \quad (8)$$

In this relation, V_a was set to the theoretical maximum fibre packing for hexagonal stacking of cylinders, $V_a = \pi/(2\sqrt{3})$.

Compaction experiments

The compaction behaviour of the sample was tested using a Zwick 1474 universal testing machine mounted with a 100 kN load cell, see Fig. 4. Two circular steel plates ($\varnothing = 135$ mm) were fitted to the crosshead of the testing machine. In the experiments, the crosshead was set to move with a constant velocity, $\dot{h}$, which meant that the sample was compacted with a constant linear strain rate. For all tests, virgin samples were used. The dimensions of the samples were 250×150 mm^2. This means the samples were larger than the circular steel plate and the testing area was not exposed to the powder soluble used for the sample preparation. The compliance of the testing machine was measured by conducting a test with no sample in place, which was used to compensate the measured deflection in all results presented. The dimensions and weight of all samples were measured before the tests, to calculate the areal weight and fibre volume fraction (cf. Eq. 2).

[Figure 4 around here]

As discussed in the introduction, Gutowski et al.[5,6] presented in early research models which are capable of capturing the quasi-static response of a fibrous material being compacted. As fibrous materials are normally subject to subsequential unloading, such models are inadequate for these applications. To allow for the inclusion of a subsequent unloading step, Michaud and Månson[12] fitted a high-order polynomial to data from single-step compaction experiments. While a high-order polynomial gives the freedom to fit virtually any data, we found that this approach tended to overfit the data from our experiments. To cope with this issue, we instead used a linear combination of power-laws. The benefit of this as compared to a high-order polynomial is that power-laws are well-representative of the physics of compacting a fibrous material. As the early model suggested by Gutowski et al.[5,6], a power-law has asymptotic limits when constructed correctly, such that $\sigma \to 0$ when $V_f \to 0$ and $\sigma \to \infty$ when $V_f \to V_a$.

For the loading history of samples, a single three-parameter power-law was fitted:

$$\sigma = A_s(V_f - V_0)^{n_1} \tag{9}$$

Following the terminology in Gutowski et al.[5,6], A_s holds the spring stiffness of the fibrous material, V_0 is the volume fraction of the free-standing fibrous material, and n_1 is the power-law exponent. In this study, A_s, V_0, and n_1 were all treated as fitting parameters.

Once these fitting parameters have been determined based on the loading history of the samples, three additional parameters were fitted to the unloading history. We found a single power-law inadequate of capturing this response, whereby a linear combination of two power-laws was used to characterise the unloading history:

$$\sigma = k_1\sigma_c\left(\frac{V_f - V_0}{V_{fc} - V_0}\right)^{n_2} + (1-k_1)\sigma_c\left(\frac{V_f - V_0}{V_{fc} - V_0}\right)^{n_3} \quad (10)$$

where n_2 and n_3 are power-law exponents, k_1 is a constant describing the mixture ratio between the two power-laws, σ_c is the stress state of the sample before unloading, and V_{fc} is the corresponding volume fraction calculated using Eq. (9). In Fig. 5, Eqs. (9-10) are plotted for some selected compaction/decompaction levels.

To summarize, Eqs. (9-10) present an approach to include the inelastic response of a fibrous material loaded in a single compaction/decompaction step without considering plasticity explicitly. Finally, it is noted that no viscoelastic or viscoplastic effects are considered, which means Eqs. (9-10) are only valid for quasi-static loading or the specific strain rate applied in the compaction experiments.

[Figure 5 around here]

Results and discussions

Following the procedures in the previous section, the experimental characterisation of the permeability and compaction behaviour is described in this section. To establish a basis for discussing the effect of texturisation, experiments of both air-texturised and UD-rovings were carried out, see Table 1.

[Table 1 around here]

Permeability experiments

Following the test conditions given in Table 2, radial impregnation tests were conducted of twelve samples of air-texturised fibres. As listed in Table 1, the air-texturised roving was a commercial material acquired from the industrial vendor "Vetrotex Saint Gobain". The results are plotted and compared to nominal and best fit fibre radii from Eq. (8), in Fig. 6 and Table 3. The mean value of the permeability and fibre volume fraction, together with coefficients of variation, c_v*, are listed in Table 4. Typical pressure histories and the evolution of the principal permeabilities and direction, K_1, K_2, and ψ, are examplified for one sample in Appendix B.

*c_v = std. deviation/arithmic mean

[Tables 2, 3, and 4 around here]

Conventional UD-rovings In addition to the experiments of air-texturised rovings, twelve reference experiments of conventional UD-rovings were conducted as well. However, this fibre configuration showed a strongly anisotropic behaviour. In fact, based on the shape of the elliptic imprint from the test fluid on the bottom plate of the permeability cell, a degree of anisotropy of approximately $\alpha = K_1/K_2 \approx 100$ was obtained[†]. As the test fluid only reached a single pressure sensor during the test, there was not enough basis for determining the principal permeabilities based on these experiments. For the purpose of comparison, normalised permeabilities from Bezerra et al.[31,32] are plotted in Fig. 7. Please note that Bezerra et al.[31,32] reported a similar magnitude of anisotropy for their experiments on conventional UD-rovings.

Analysis of results From the results listed in Table 4, it can be read that the characteristic value, c_v, varied from 0.63% to 1.05% wrt. the fibre volume fraction of the samples. This is on par with what was reported by participants in a recent benchmark exercise by May et al.[29]. For the principal permeability along the fibre direction, K_1, a c_v-value between 14.41% to 28.20% was obtained. For K_2, this was between 12.20% to 21.57%. In both these cases, the highest c_v value was obtained for the experiments with high V_f. As this configurations required the highest compaction pressure and had the smallest cavity thickness, this was to be expected. Finally, based on the angle of the principal axis indicated in Fig. 6, there was no noticeable bias of the principal direction to report.

While the c_v-values for the permeability results are higher than what was on average reported in the benchmark exercise by May et al.[29] (7.8% to 12.2%, depending on fabric type), it is still on the same level or lower than several individual participants. Bearing in mind that participants in the benchmark exercise[29] tested a mass-manufactured commercial technical fabric, the c_v-values in this study demonstrated reasonable repeatability and control of variations.

To compare the permeability of an air-texturised roving to a conventional UD-roving, results were compared to the experimental results from Bezerra et al.[31,32]. In their work, a layup of single rovings was guided

[†]This was based on (Length of elliptical imprint/width of elliptical imprint)$^2 \approx 100$

into a permeability cell using perforated plates. Similar to this paper, their permeability characterisation was also completed by conducting radial injection tests with pressure sensors monitoring the impregnation flow. Compared to Bezerra et al.'s results, the normalised permeability of the air-texturised roving was approximately three times higher along the fibre direction, K_1, and 40 times higher transverse to the fibre direction, K_2 (cf. Fig. 7). For reference, when compared to Gebart's empirical model[21], the permeability was four times higher for K_1 and three times higher for K_2 (cf. Fig. 6). It is clear that air-texturisation increases permeability. This follows the expected behaviour, as the texturisation introduces disorder in the fibre architecture, which increases the permeability[25,26]. In addition to increasing the permeability, the degree of anisotropy was decreased with approximately one magnitude as well.

While the disorder in fibre architecture increases the permeability, the texturisation introduces out-of-plane fibres. Compared to the conventional UD-roving, the flow now needs to pass additional fibres in the $1-$direction, which increases the flow resistance. In the $2-$direction, the texturisation has the opposite effect; the additional out-of-plane fibres means fewer fibres to pass, which decreases the resistance for flow. The increase in permeability in the $2-$direction was significant (40 times). It is noted that the resin may travel in less fibre-rich areas between fibre agglomerations, which can be a contributing factor to the increase in permeability.

[Figures 6 and 7 around here]

Compaction experiments

Compaction experiments were conducted on virgin samples of air-texturised rovings as well as conventional UD-rovings (cf. Table 1). The experimental results are compared to best-fits of Eqs. (9-10) in Fig. 8, and the best-fit parameters are listed in Table 3. In addition, selected points during unloading are compared to curve fits in Fig. 9. A summary of test conditions is listed in Table 5.

[Table 5 around here]

Analysis of results Statistical analysis of the results was conducted by comparing the obtained load-displacement curves at selected points. These points were the volume fractions obtained when the given material was subject to a compaction pressure of $\sigma = 1$ bar and $\sigma = 5$ during loading. The mean and characteristic values, c_v, are listed in Table 6. The characteristic values were low, ranging from $\pm 0.9\%$ (air-text. at $\sigma = 5$ bar) to $\pm 2.1\%$ (conv. UD-rovings at $\sigma = 1$ bar). In both cases, the characteristic value was higher for low compaction pressure and lowest for the air-texturised roving.

[Table 6 around here]

At a compaction pressure of $\sigma = 1$ bar, the conventional UD-rovings were compressed to a volume fraction of $V_f = 0.51$. For the air-texturised roving, this was 33% lower at $V_f = 0.34$. At $\sigma = 5$ bar, these numbers were $V_f = 0.60$, $V_f = 0.43$, (air-texturised roving 29% lower). As the results indicate, the compaction pressure needed to achieve a certain volume fraction was significantly higher for the air-texturised roving. Gutowski et al.[5,6] hypothesised that a disordered fibre architecture *"moves the graphs [load-displacement curves] to the left"*. Indeed, this is the case when comparing conventional UD-rovings to air-texturised rovings in Fig. 8. It is not surprising that texturisation results in a less compliant roving, as individual fibres simply cannot be as densely packed in a disordered fibre architecture. Consequently, a higher restoring force is achieved when subject to compaction.

While both conventional UD-rovings and air-texturised rovings gradually build up a restoring force when loaded, the decompaction behaviour of the two roving types was different (cf. Fig. 8). Both types exhibited reduced restoring force when unloaded, but the decompaction curve of conventional UD-rovings appeared almost vertical. Consequently, the observed hysteresis for conventional UD-rovings was more substantial, which reflects a more distinct inelastic or plastic behaviour. When the fibrous material is subject to loading, individual fibres are bent as noted by Gutowski et al.[5,6]. In addition, irreversible deformation may take place as a result of individual fibres permanently moving and reorganising to accommodate a more dense fibre packing[19]. The latter behaviour characterises inelastic or plastic behaviour, which the results indicate was more prominent for the conventional UD-roving. The disordered fibre architecture of the air-texturised rovings gives a skeleton-like structure that constrains fibres from permanently moving and reorganising and instead "bounce back" when unloaded. Arguably, this is the reason for the lower hysteresis observed for the air-texturised roving.

Closing remarks

Based on the results presented in this section, applying texturisation adds features to rovings that are desirable in many LCM processes and for fibre-reinforced polymer composites in general.

The increased permeability, for example, allows for faster impregnation in LCM processes. In pultrusion processes, this means a profile can be drawn at a faster pulling speed, which allows for increased production output. In addition, the lower degree of anisotropy means a pultrusion die can be shorter by design because a low degree of anisotropy introduces less resin backflow. On the other hand, the X-ray, μ-CT scans in Fig. 1 showed that texturisation results in local areas with fibre agglomerations. This introduces fibre-rich areas that can be difficult to saturate. Ultimately, this can increase the risk of local voids.

The compaction behaviour showed that composite parts prepared with air-texturised rovings will have a lower volume fraction when subject to a certain compaction pressure. Depending on the resin system and the cost of the texturisation step, this can translate into a lower cost of the end product.

Although it was not investigated in this paper, texturisation will affect the mechanical properties of a composite part. In addition to achieving a lower fibre volume fraction, the μ-CT scans in Fig. 1 illustrate that texturisation orient fibres away from the principal direction. This alteration reduces axial stiffness and strength of the composite part, which can be undesirable if a design can take advantage of a high degree of mechanical anisotropy. On the other hand, texturisation results in a disordered and intermingled fibre architecture, which increases out-of-plane properties such as fracture toughness as well as transversal and shear stiffness and strength.

[Figures 8 and 9 around here]

Conclusion

This study concerned material characterisation of air-texturised glass-fibre rovings. Motivated by a gap in the research field, the scope of the paper was to characterise material properties needed for input in liquid composite moulding (LCM) simulations, i.e. the permeability and compaction behaviour.

For characterisation of the permeability, a special rig was built to prepare individual rovings into a ply-like sample. Once samples were made this way, an existing setup designed for radial impregnation tests of fabrics and mats could be used. For compaction tests, samples were tested in a universal testing machine. A linear combination of power-laws was used as a model capable of capturing irreversible fibre-compaction valid for a single loading/unloading step. With the main application of pultrusion processes in mind, curve fits were compiled for implementation in simulation software.

We highlight the following findings and conclusions of the material characterisation study:

- Compared to conventional unidirectional (UD) rovings, the normalised permeability of the air-texturised roving was approximately three times higher along the fibre direction and 40 times higher transverse to the fibre direction. Accordingly, the degree of anisotropy was approximately one magnitude lower;
- At a compaction pressure of 1 and 5 bar, the air-texturised roving was compressed to a volume fraction of $V_f = 0.34$ and 0.43, respectively, which was approximately 30% lower than the volume fractions achieved for the conventional UD-rovings;
- Compared to conventional UD-rovings, decompaction of air-texturised rovings showed a more distinct elastic response when unloaded.

In summary, it is concluded that air-texturisation increases the permeability and decreases compliance of rovings.

A topic for future research could be to standardise and characterise different degrees of texturisation. Possible extensions of this study could explore the effects of air flow, nozzle shape and size, exposure time in the texturisation step. In addition, possible topics could involve how mechanical or thermal properties of composite parts are affected by the anisotropy caused by texturisation.

Acknowledgements

This work is funded by the Danish Council for Independent Research — Technology and Production Sciences (Grant no. DFF-6111-00112: Modelling the multi-physics in resin injection pultrusion (RIP) of complex industrial profiles).

References

1. Starr T. *Pultrusion for Engineers*. Taylor & Francis, 2000. ISBN 9780849308437.
2. Sandberg M, Hattel JH and Spangenberg J. Numerical modelling and optimisation of fibre wet-out in resin-injection pultrusion processes. In *European Conference on Composite Materials*, volume 18. Athens, Greece.
3. Sandberg M, Hattel JH and Spangenberg J. Simulation of liquid composite moulding using a finite volume scheme and the level-set method. *International Journal of Multiphase Flow* 2019; 118: 183–192.
4. Sandberg M, Rasmussen FS, Hattel JH et al. Simulation of resin-impregnation, heat-transfer and cure in a resin-injection pultrusion process. *AIP Conference Proceedings* 2019; 2113(1): 20022.
5. Gutowski TG, Cai Z, Bauer S et al. Consolidation Experiments for Laminate Composites. *Journal of Composite Materials* 1987; 21(July): 650–669.
6. Gutowski TG, Morigaki T and Cai Z. The Consolidation of Laminate Composites. *Journal of Composite Materials* 1987; 21(2): 172–188.
7. Robitaille F and Gauvin R. Compaction of textile reinforcements for composites manufacturing. ii: Compaction and relaxation of dry and h2o-saturated woven reinforcements. *Polymer composites* 1998; 19(5): 543–557.
8. Saunders R, Lekakou C and Bader M. Compression in the processing of polymer composites 1. a mechanical and microstructural study for different glass fabrics and resins. *Composites Science and Technology* 1999; 59(7): 983–993.
9. Chen ZR and Ye L. A micromechanical compaction model for woven fabric preforms. part ii: Multilayer. *Composites Science and Technology* 2006; 66(16): 3263–3272.
10. Comas-Cardona S, Le Grognec P, Binetruy C et al. Unidirectional compression of fibre reinforcements. part 1: A non-linear elastic-plastic behaviour. *Composites science and technology* 2007; 67(3-4): 507–514.
11. Saunders R, Lekakou C and Bader M. Compression in the processing of polymer composites 1. A mechanical and microstructural study for different glass fabrics and resins. *Composites Science and Technology* 1999; 59(7): 983–993.
12. Michaud V and Månson JAE. Impregnation of compressible fiber mats with a thermoplastic resin. Part I: Theory. *Journal of Composite Materials* 2001; 35(13): 1150–1173.
13. Michaud V and Mortensen A. Infiltration processing of fibre reinforced composites: Governing phenomena. *Composites - Part A: Applied Science and Manufacturing* 2001; 32(8): 981–996.

14. Comas-Cardona S, Le Grognec P, Binetruy C et al. Unidirectional compression of fibre reinforcements. Part 1: A non-linear elastic-plastic behaviour. *Composites Science and Technology* 2007; .
15. Cheng JJ, Kelly PA and Bickerton S. A rate-independent thermomechanical constitutive model for fiber reinforcements. *Journal of Composite Materials* 2012; .
16. Kelly PA. A viscoelastic model for the compaction of fibrous materials. *Journal of the Textile Institute* 2011; .
17. Danzi M, Schneeberger C and Ermanni P. A model for the time-dependent compaction response of woven fiber textiles. *Composites Part A: Applied Science and Manufacturing* 2018; 105: 180–188.
18. Somashekar AA, Bickerton S and Bhattacharyya D. Exploring the non-elastic compression deformation of dry glass fibre reinforcements. *Composites Science and Technology* 2007; .
19. Kabachi MA, Danzi M, Arreguin S et al. Experimental study on the influence of cyclic compaction on the fiber-bed permeability, quasi-static and dynamic compaction responses. *Composites Part A: Applied Science and Manufacturing* 2019; 125(April): 105559.
20. Carman PC. Fluid flow through granular beds. *Trans Inst Chem Eng* 1937; 15: 150–166.
21. Gebart BR. Permeability of Unidirectional Reinforcements for RTM. *Journal of Composite Materials* 1992; 26(8): 1100–1133.
22. Cai Z and Berdichevsky AL. An improved self-consistent method for estimating the permeability of a fiber assembly. *Polymer Composites* 1993; 14(4): 314–323.
23. Berdichevsky AL and Cai Z. Preform permeability predictions by self-consistent method and finite element simulation. *Polymer Composites* 1993; 14(2): 132–143.
24. Van der Westhuizen J and Prieur Du Plessis J. An attempt to quantify fibre bed permeability utilizing the phase average Navier-Stokes equation. *Composites Part A: Applied Science and Manufacturing* 1996; 27(4): 263–269.
25. Lundström TS and Gebart BR. Effect of Perturbation of Fibre Architecture on Permeability Inside Fibre Tows. *Journal of Composite Materials* 1995; 29(4): 424–443.
26. Shou D, Fan J and Ding F. Hydraulic permeability of fibrous porous media. *International Journal of Heat and Mass Transfer* 2011; 54(17-18): 4009–4018.

27. Arbter R, Beraud J, Binetruy C et al. Experimental determination of the permeability of textiles: A benchmark exercise. *Composites Part A: Applied Science and Manufacturing* 2011; 42(9): 1157–1168.
28. Vernet N, Ruiz E, Advani SG et al. Experimental determination of the permeability of engineering textiles: Benchmark II. *Composites Part A: Applied Science and Manufacturing* 2014; 61: 172–184.
29. May D, Aktas A, Advani SG et al. In-plane permeability characterization of engineering textiles based on radial flow experiments: A benchmark exercise. *Composites Part A: Applied Science and Manufacturing* 2019; 121(October 2018): 100–114.
30. Schell JS, Siegrist M and Ermanni P. Experimental determination of the transversal and longitudinal fibre bundle permeability. *Applied Composite Materials* 2007; 14(2): 117–128.
31. Bezerra RM, Wilhelm F and Henning F. Compressibility and Permeability of Fiber Reinforcements for Pultrusion. In *16th European Conference on Composite Materials*, volume 22-26 June. ISBN 9780000000002.
32. Bezerra RM, Henning F and Drechsler K. *Modelling and Simulation of the Closed Injection Pultrusion Process*. Phd thesis, Karlsruher Institut fur Technologie (KIT), 2017.
33. Rasmussen FS, Emerson MJ, Sonne MR et al. Fiber segmentation from 3D X-ray computed tomography of composites with continuous textured glass fibre yarns. In *Proceedings of 2019 International Conference on Tomography of Materials & Structures*.
34. Louis BM, Di Fratta C, Danzi M et al. Improving time effective and robust techniques for measuring in-plane permeability of fibre preforms for lcm processing. In *Proceedings 2011 SAMPE Europe International Conference Paris*. Society for the Advancement of Material and Process Engineering, pp. 204 – 211.
35. Chan AW and Hwang STT. Anisotropic in-plane permeability of fabric media. *Polymer Engineering & Science* 1991; 31(16): 1233–1239.
36. Weitzenböck JR, Shenoi RA and Wilson PA. Radial flow permeability measurement. Part A: Theory. *Composites Part A: Applied Science and Manufacturing* 1999; 30(6): 781–796.

Appendix A. X-ray, μ-CT scans

The X-ray micro computed tomography images (X-ray, μ-CT) were captured using a Zeiss Xradia Versa 520 scanner. The specimens for scanning were prepared by cutting out cylindrical samples from composite parts. Each sample was subsequently reduced to a diameter of $\varnothing 5$ mm using a lathe. The scans were carried out at a voltage of 40kV and a power of 74 μA using $4\times$ optical magnification. Each scan was performed using 4501 projections at binning 2 with a total scanning time of 20 hours. For each cutout, the scan was further cropped to a $\varnothing 2 \times 2$ mm cylinder. The resulting scans in Fig. 1 have a 1000^3 voxel resolution with a voxel size of approxiamtely 2 μm. For more information about the scanning procedure, please see Rasmussen et al.[33].

Appendix B. Example of probed pressure histories

Figure 10 exemplify pressure readings and the associated evolution of principal permeabilities and direction, for one permeability experiment used as a data point in Figs. 6 and 7. The sample was prepared from air-texturised rovings (cf. Table 1). The cavity thickness in the permeability cell was set to $h = 1.6$ mm, which resulted in a volume fraction of $V_f = 0.379$. The inflow rate was set to $Q = 10^{-7}$ m^3/s, whereby the impregnation time lasted for approximately seven minutes.

[Figure 10 around here]

List of Figures

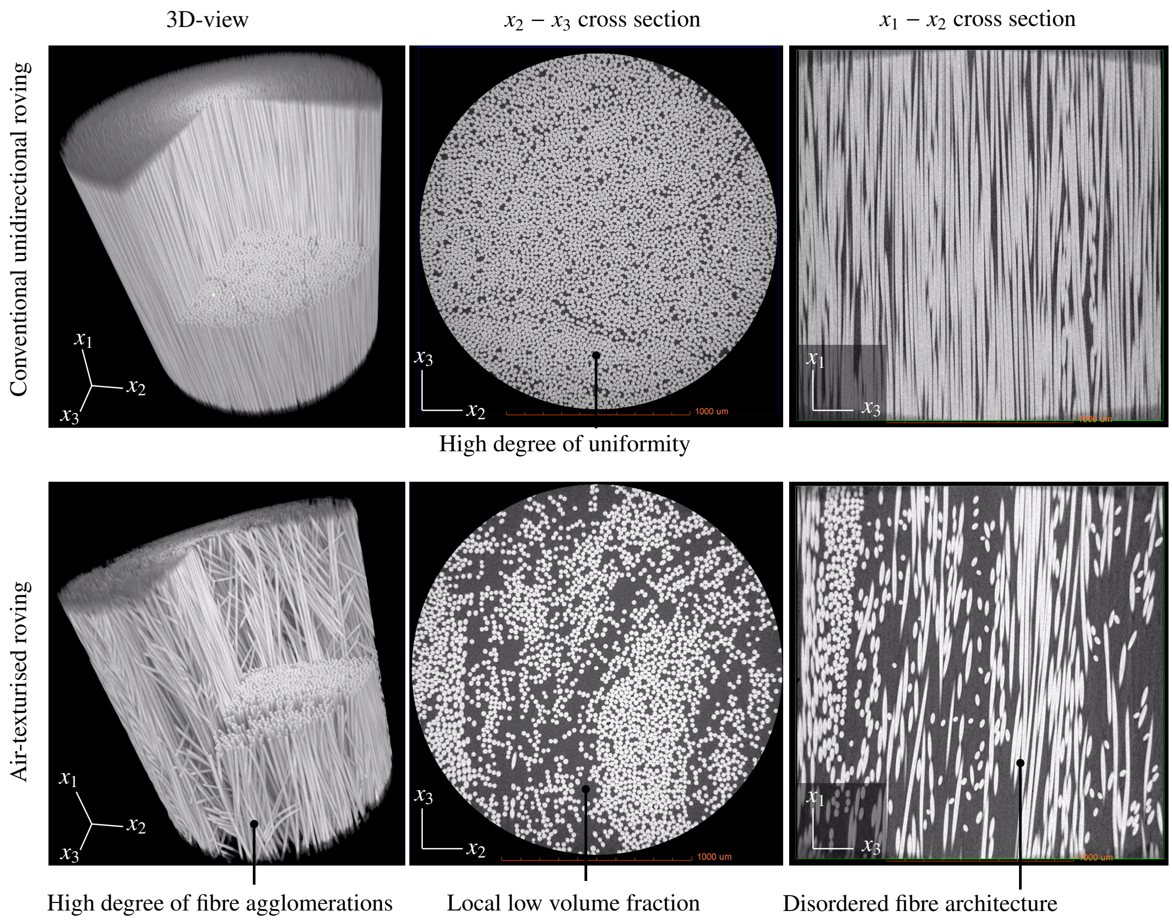

Figure 1. 3D and cross-sectional views of cutouts from a composite part manufactured using conventional UD-rovings and air-texturised rovings. The images were prepared by use of X-ray μ-CT, see Appendix A.

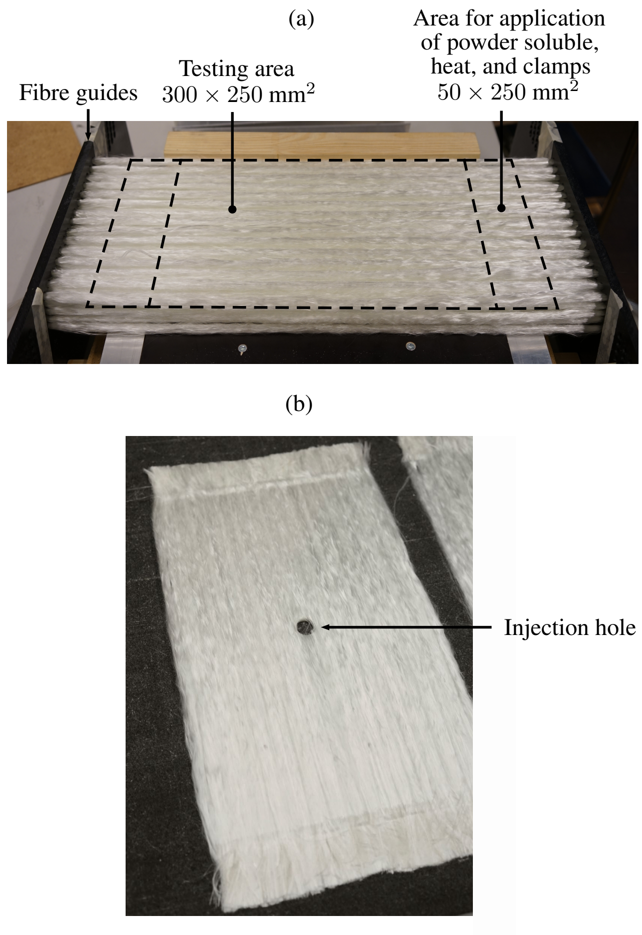

Figure 2. (a) Rig for sample preparation. (b) One prepared sample (air-texturised rovings) for impregnation tests.

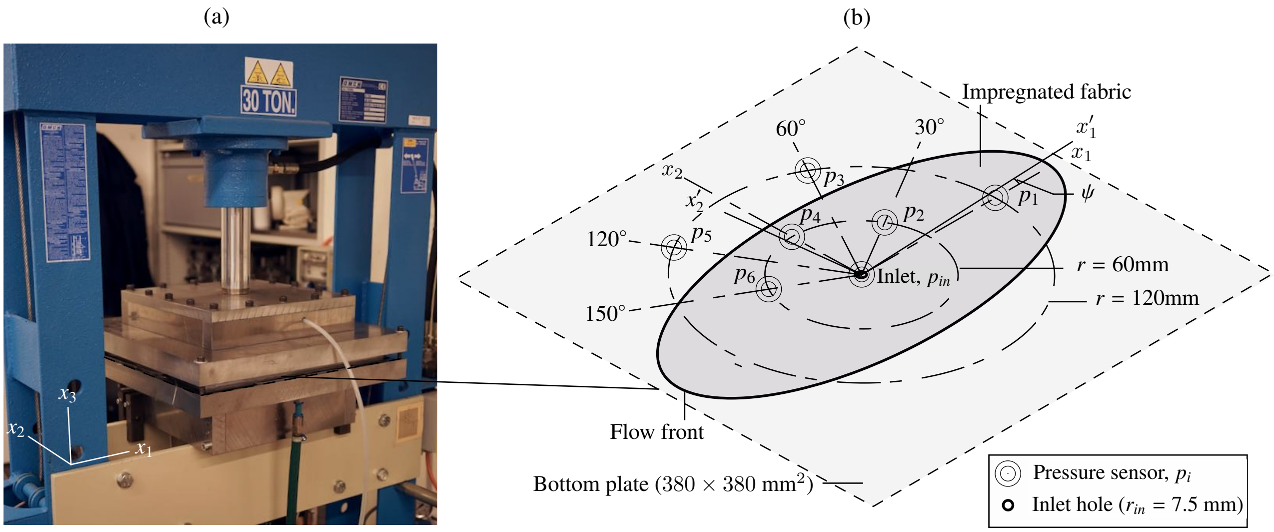

Figure 3. (a) Permeability measurement cells designed for radial impregnation tests. (b) Schematic of the pressure sensors and the radial flow that takes place inside the cavity of the permeability cell.

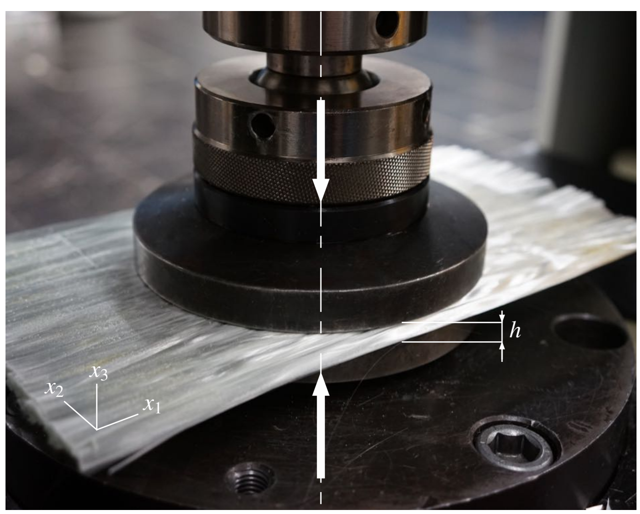

Figure 4. Sample (conventional UD roving) for compaction tests placed between circular steel discs mounted in a universal testing machine.

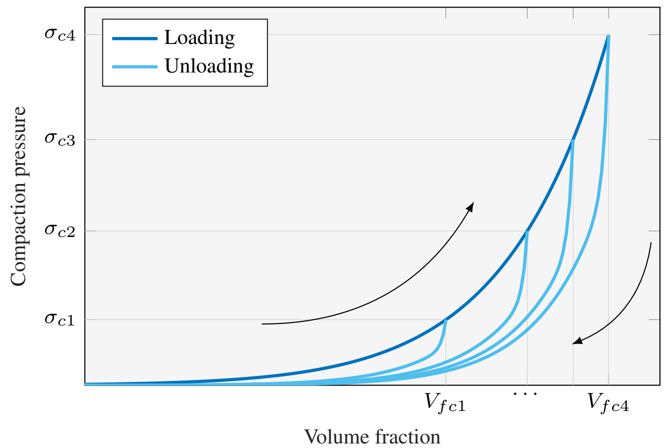

Figure 5. Example of compaction-decompaction curve fitted using Eqs. (9-10). The levels, V_{fci}, σ_{ci}, corresponds to the compaction level of sample i before unloading.

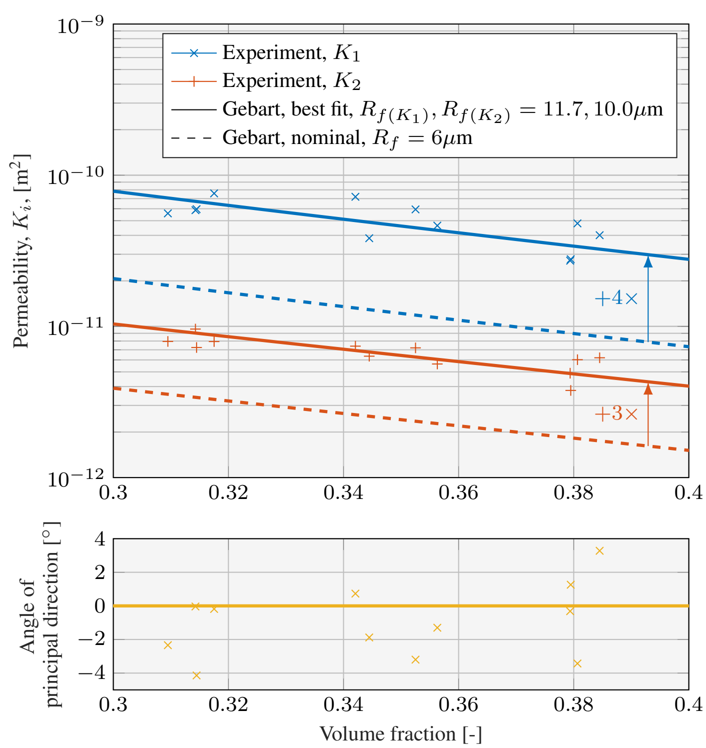

Figure 6. Experimental results of measured the permeability of air-texturised roving. Comparison of nominal and best-fit fibre radii from Eq. (8) (cf. Gebart[21]). Multiples are approximate.

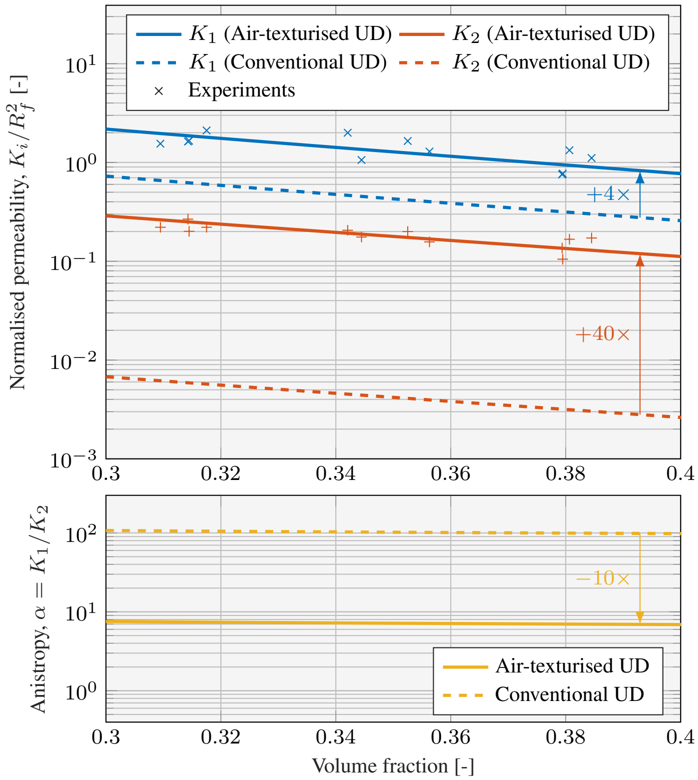

Figure 7. Comparison of the permeability of air-texturised rovings vs. conventional rovings. Curves for air-texturised rovings are based on best-fit fibre radii from Eq. (8) (c.f. Gebart[21]). Data for conventional UD-rovings are based on Bezerra et al.[31,32], where the nominal fibre radius was $R_f = 12\ \mu$m, and best-fit radii were, $R_{f(K_1)}, R_{f(K_2)} = 13.5, 3.5\ \mu$m. Multiples are approximate.

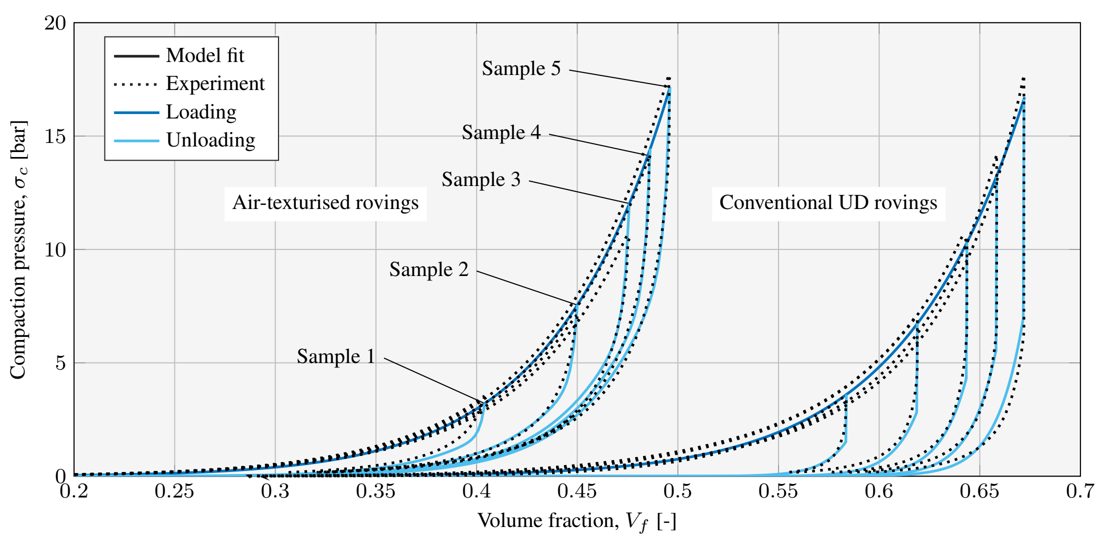

Figure 8. Applied compaction pressure, σ, vs. measured volume fraction, V_f, compared to model fit, Eqs. (9-10).

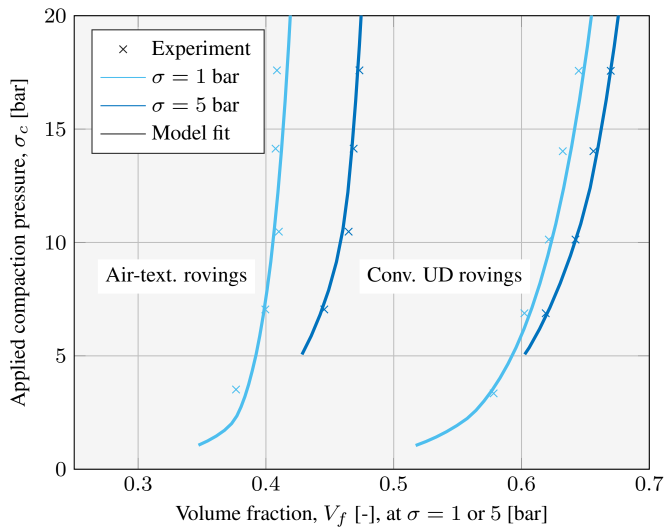

Figure 9. Comparison between model fit, Eqs. (9-10), and experimental data for unloading after application of compaction pressure, σ_c.

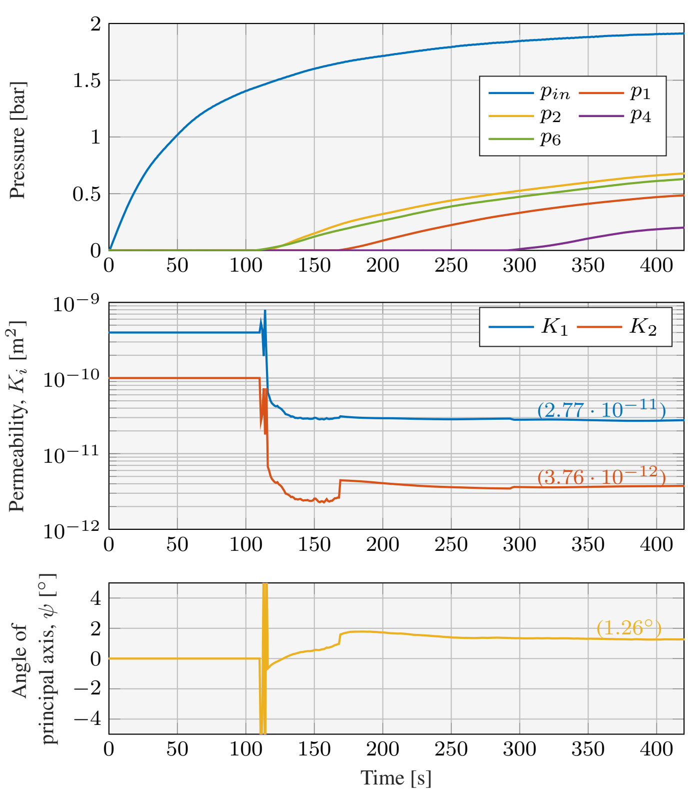

Figure 10. Example of pressure readings from one permeability experiment used as a data point in Figs. 6 and 7. The sensor locations are depicted in Fig. 10.

List of Tables

Table 1. Overview of roving types.

Material name	Conventional UD-roving	Air-texturised roving
Vendor (and type)	Mühlmeier Composites	Vetrotex ECO14 5000 T10C
Glass type	E-glass	E-glass
Fibre radius, r_f, [μm]	11	6
Tex [g/km]	4800	5000

Table 2. Parameters for the test setup used in permeability experiments.
[1] The constant injection rate was chosen wrt. to the cavity thickness and the volume fraction such that the impregnation time lasted approximately seven minutes.

Parameter	Quantity
Sample dimensions	380×250 [mm×mm]
Test fluid and viscosity	Bluesil 47 V 100, $\mu = 0.1$ Pa·s
Cavity thickness, h	$1.6 - 2$ [mm]
Volume fraction of samples	$0.31 - 0.38$ [-]
Approx. number of rovings in each sample	70
Injection rate[1]	$1 - 1.4 \cdot 10^{-7}$ [m^3/s]
No of samples	12 samples

Table 3. Compiled best-fit based on the experimental data. **Refers to data from Bezerra et al.*[31,32].

	Conventional UD-roving	Air-texturised roving
Principal permeabilities, cf. Eq. (8)		
Best-fit fibre radii, $R_{f(K_1)}, R_{f(K_2)}$	$13.5, 3.5$ μm*	$11.7, 10.0$ μm
Compaction/decompaction, cf. Eqs. (9-10)		
Spring constant, A_s	0.31 [bar]	2.01 [bar]
Reference volume fraction, V_0	-0.54 [-]	-0.62 [-]
Ratio between power-laws, k_1	0.43 [-]	0.58 [-]
Power-law exponents, n_i	$20.21, 9.18 \cdot 10^3, 2.74 \cdot 10^6$ [-]	$19.49, 3.01 \cdot 10^3, 4.30 \cdot 10^4$ [-]

Table 4. Mean volume fractions and principal permeabilities, together with characteristic values, c_v, of air-texturised roving (cf. Table 1). Four samples were tested for each configuration.

Configuration	V_f ($\pm c_v$) [-]	K_1 ($\pm c_v$) [10^{-11} m^2]	K_2 ($\pm c_v$) [10^{-11} m^2]
Low V_f	0.31 ($\pm$1.05%)	6.25 ($\pm$14.41%)	0.82 ($\pm$12.20%)
Mid V_f	0.35 ($\pm$1.91%)	5.40 ($\pm$27.40%)	0.67 ($\pm$12.24%)
High V_f	0.38 ($\pm$0.63%)	3.58 ($\pm$28.20%)	0.52 ($\pm$21.57%)

Table 5. Test paramaters for compaction/decompaction experiments.

Parameter	Quantity
Sample dimensions	250×150 mm^2
Diameter of compaction plates	$\varnothing = 135$ mm
Applied load/pressure before unloading (σ_c)	5-20 kN/3.3-17.6 bar
Applied displacement rate, $\dot{h}$	2 mm/min
Number of samples	5 samples

Table 6. Mean value of volume fractions achieved at certain stress levels during loading of the materials tested. c_v refers to the characteristic value.

	V_f ($\pm c_v$) at $\sigma = 1$ bar	V_f ($\pm c_v$) at $\sigma = 5$ bar
Conventional UD roving	0.51 ($\pm$2.1%)	0.60 ($\pm$1.0%)
Air-texturised roving	0.34 ($\pm$1.3%)	0.43 ($\pm$0.9%)